Progress in the study of warm dense matter

View the article online for updates and enhancements.

Progress in the study of warm dense matter

**M Koenig[1], A Benuzzi-Mounaix[1], A Ravasio[1], T Vinci[1], N Ozaki[1],
S Lepape[1], D Batani[2], G Huser[3], T Hall[4], D Hicks[5], A MacKinnon[5],
P Patel[5], H S Park[5], T Boehly[6], M Borghesi[7], S Kar[7] and L Romagnani[7]**

[1] Laboratoire pour l'Utilisation des Lasers Intenses, UMR7605, CNRS—CEA-Université Paris VI-Ecole Polytechnique, 91128 Palaiseau Cedex, France
[2] Dipartimento di Fisica 'G. Occhialini', Università di Milano-Bicocca and INFM, Piazza Della Scienze 3, 20126 Milano, Italy
[3] CEA DRIF, BP 12, 91680 Bruyères-le-Châtel, France
[4] Physics Centre, University of Essex, Colchester CO4 3SQ, UK
[5] Lawrence Livermore National Laboratory, Livermore, CA 94550, USA
[6] Laboratory for Laser Energetics, University of Rochester, USA
[7] Department of Physics and Astronomy, Queen's University of Belfast, UK

Abstract

In the last few years, high power lasers have demonstrated the possibility to explore a new state of matter, the so-called warm dense matter. Among the possible techniques utilized to generate this state, we present the dynamic compression technique using high power lasers. Applications to planetary cores material (iron) will be discussed. Finally new diagnostics such as proton and hard-x-ray radiography of a shock propagating in a solid target will be presented.

(Some figures in this article are in colour only in the electronic version)

1. Introduction

The so-called warm dense matter (WDM) is a state of matter which lies at the frontiers between condensed matter and plasma physics. Here the density goes from solid density up to 10 times its value; the temperature varies from 0.1 to 100 eV. In this regime, matter is mostly degenerate ($T \leqslant T_f \prec n_e^{-2/3}$), strongly coupled ($\Gamma \prec (T_f n_e^{1/3})^{-1}$) and non ideal. WDM is part of the so-called high energy density physics (HEDP) which includes a wide variety of physical phenomena. *'The energy density of common, room-temperature materials provides a starting point for a definition of high energy density conditions. Many of these materials (such as hydrogen, carbon, water and iron) are ubiquitous in the universe. One definition of high energy density conditions is that these conditions exist when the external energy density applied to the material is comparable to the material's room temperature energy density. For example, the bulk modulus of solid or liquid-state materials is ranging*

from 10^9 to 10^{11} J m^{-3}' (see [1]). These extreme conditions are non trivial to simulate either theoretically, numerically or experimentally. From the theory point of view, one has to deal with *ab initio* calculations [2] (molecular dynamics) which work well at low temperatures ($T < 1$ eV) or variational methods [3,4] (density functional theory) which can be very efficient in a plasma phase. However for most of the WDM 'phase diagrams', these methods are pushed to their intrinsic limits and experiments are the only way to discriminate between the theories. Therefore, the key issue is to create those conditions in the laboratory which is still a challenge. Several techniques are used to achieve WDM state among which are diamond anvil cell (DAC), gas guns and high power lasers. They are mostly devoted to equation of state (EOS) of highly compressed matter which is of fundamental interest to several branches of physics, including astrophysics [5], geophysics [6] and inertial confinement fusion (ICF) [7]. In this paper, we shall focus on this particular topic within WDM physics, first by illustrating the state of the art on materials which have important implications in planet cores physics. In the case of water (Neptune and Uranus iced layer) for example, the bulk modulus is $\approx 2 \times 10^9$ J m^{-3} which means that, considering the typical volume involved in laser targets ($< 10^{-9}$ m^3), less than a few joules will bring the sample in HEDP state. For iron, the main constituent of the Earth, the bulk modulus is quite high (about 100 times the water value), which means that a higher energy laser is needed to generate a WDM state. In this paper we first describe a laser shock wave experiment dedicated to an absolute EOS measurement of iron in the range of pressures 1–7 Mbar. Here we determine the shock and fluid velocities on the same shot using self-emission diagnostic and a VISAR as previously described in lasers experiments [8]. In order to achieve iron melting temperature under compression, we performed several experiments using a LiF window (which remains transparent up to 400 GPa), looking therefore to a release state of iron in the LiF. We first measured the interface velocity which then acts as a pressure gauge. Then we determined temperature using a method already used in other experiments [9].

Finally, recent developments using proton or hard x-ray radiography will be presented.

2. Iron as a paradigm

Knowledge of the phase diagram of iron is a fundamental issue in geophysics. In particular its melting line locus in the vicinity of the inner core–outer core boundary (IOB) pressure for the earth of 3.3 Mbar yields a better understanding of the core's thermodynamics. Static measurements of the melting line can be achieved with good precision [10] but need to be extrapolated above about 1 Mbar. The use of dynamic compression techniques is therefore necessary.

To that extent, we performed measurements along the iron principal Hugoniot using the LULI high power laser in order to determine important parameters such as shock and particle velocities (for the EOS absolute data) and temperature at the point where the Hugoniot crosses the melting line. We expected to measure a plateau on the Hugoniot curve from which we will deduce a melting temperature upon shock loading.

2.1. Absolute EOS measurements

For the absolute EOS measurements, we designed a specific target scheme. The targets were made of a pure iron foil whose thickness was determined by numerical simulations in order to ensure a steady shock. For our laser conditions, the total thickness was ranging from 12–18 μm. Then a mask with a grid was superimposed on one side and steps were obtained through ionic etching. According to the expected shock velocities in iron, the steps were made to 2.9 μm.
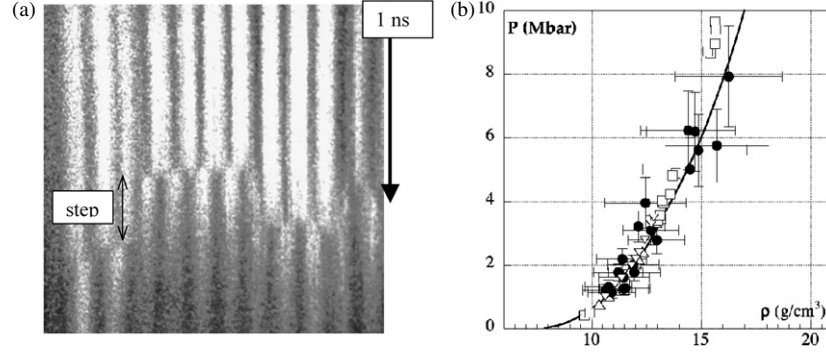
Figure 1. (*a*) Experimental image obtained with VISAR interferometer. (*b*) Experimental points on iron's principal Hugoniot (●), SESAME EOS curve (——), conventional explosions data [11–13] (□), gas gun data [14] (△) and *ab initio* calculations [15] (▽).

One of the main goals of this experiment was to measure simultaneously two velocities on the same laser shot: the shock velocity (U_s) using a know step height and the rear side velocity (V) using the VISAR diagnostic (see figure 1(*a*)).

When the shock breaks out, the rear side acquires a velocity V which can be defined as the following:

$$V = U_p - \int_{P_{Fe}}^{0} \left(-\frac{\partial V}{\partial P'} \right)_S^{1/2} dP' = U_p + U_{rw},$$

where U_{rw} is the velocity of the release wave coming back into compressed iron after the shock breaks out. One can then associate velocity V to be twice the fluid velocity (U_p) in the shock up to 2–3 Mbar in iron [16] due to its particular properties. In the limit of a weak shock wave (i.e. $(1-\rho_0/\rho) \ll 1$), where the entropy change is small, one can find from equation (1) that $U_{rw} \approx U$, thus $V \approx 2U_p$ [16]. For pressures in the range 4–8 Mbar, the weak shock limit does not apply. From the VISAR we observe the fringe displacement at the shock breakout (typically for $\approx$200 ps) and after this time the probe beam is completely absorbed by the unloading plasma. In this case, the approximation $V \approx 2U$ underestimates the real free surface velocity by 10%. When the assumption $V = 2U$ is no more valid (with more than 3% departure), we do not get anymore a good absolute EOS measurement, but rather a point on the release wave in shocked iron. However the measurement of both parameters U_s and V on the same shot allows us to get absolute EOS points on the principal Hugoniot.

The data are shown (figure 1(*b*)) in the (P, ρ) plane by using Hugoniot–Rankine relations:

$$\rho = \rho_0(1 - U_p/U_s)^{-1}. \tag{1}$$

Our experimental points show good agreement, for pressures below 8 Mbar, with theoretical data such as SESAME EOS [17] or experimental points obtained by conventional explosions and gas gun technique [13, 14]. We note also that all these data are very close to the most recent *ab initio* molecular dynamics calculation [15].

However with this technique, when compression is high, the error bars are large, which does not allow us to see clearly the difference between the SESAME EOS and the *ab initio* calculations. The errors bars have different origins such as the streak camera sweep speed, the target quality (mainly iron step height) and the fringe shift determination. Moreover with the method of deducing density from velocities (equation (1)), errors will always be very sensitive to δU_s and δU_p, and one wants to measure density directly (see section 3).
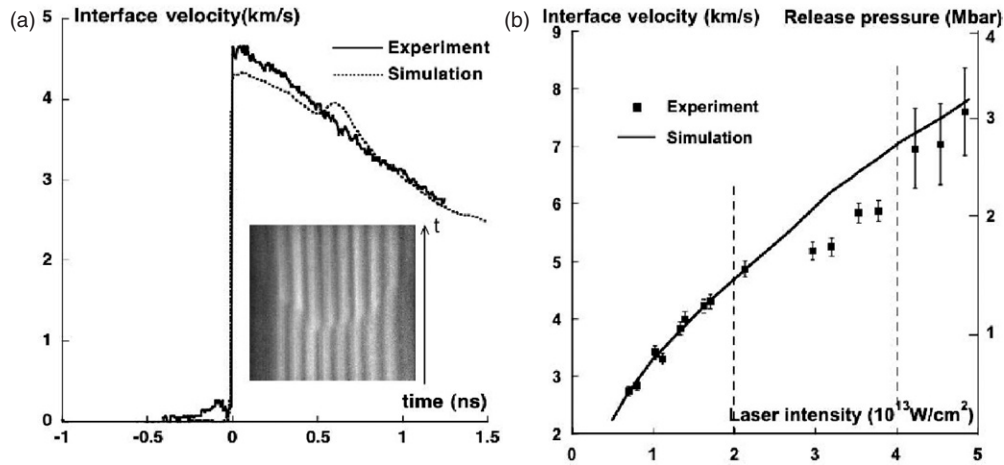
Figure 2. (*a*) Time-dependent velocity profile: experiment (——) hydrodynamic simulation (- - - -); inset shows the corresponding VISAR image. (*b*) Interface velocity as a function of laser intensity.

2.2. Melting temperature

Then, we performed a set of experiments using a rear side window. First, we measured the interface velocity and temperature of iron shock released into a LiF window. Targets were made of the first two layers of foil: a 3 μm CH ablator deposited on 12 μm of iron. We deposited 3 μm of iron using the electron beam technique on a 200 μm LiF window avoiding any glue at the interface. Finally both foils were glued together, the glue thickness being controlled to be lower than or equal to 1 μm.

The time histories of interface velocities were recorded by following fringe movement on the VISAR diagnostic. Because a shock is transmitted in the window, the measured velocity is apparent and the compressed LiF index of refraction has to be considered in order to get an accurate measurement. This is done using Kormer's model [18]:

$$n_{\mathrm{LiF}}(\sigma) = n_0 + \frac{\mathrm{d}n}{\mathrm{d}\sigma}(\sigma - 1),$$

where $\sigma = \rho/\rho_0$ is the compression. For LiF, $n_0 = 1.39$ and $\mathrm{d}n/\mathrm{d}\sigma = 0.1$. When inserting the compressed LiF index of refraction into the optical path difference expression of the probe beam, the σ terms cancel out and we find a constant factor 1.29 between the apparent velocity and the actual interface velocity.

For laser intensities below 3×10^{13} W cm^{-2} with a 700 ps square pulse, we find time histories in good agreement with a 1D hydrodynamic code for the central part of the focal spot associated intensity (figure 2(*a*)). This enables us to validate the model we use for correcting the apparent velocity. Note that the small glitch in the simulation is due to reflection shocks from a 1 μm glue between iron foil and iron deposit on the LiF window. We also compared experimental and predicted interface velocities at shock breakout as a function of laser intensity. We find discrepancies for laser intensity $>3 \times 10^{13}$ W cm^{-2} (figure 2(*b*)). The hydrodynamic code uses an EOS that does not take into account phase transitions.

We therefore attribute this drop of velocity to the consumption of latent heat of melting upon solid–liquid phase transition. However, previously published values for iron's enthalpy (internal energy + the pressure work PV) of melting at IOB [15, 19, 20] yield a velocity drop of <0.5 km s^{-1}, which is not sufficient to completely explain the discrepancies.
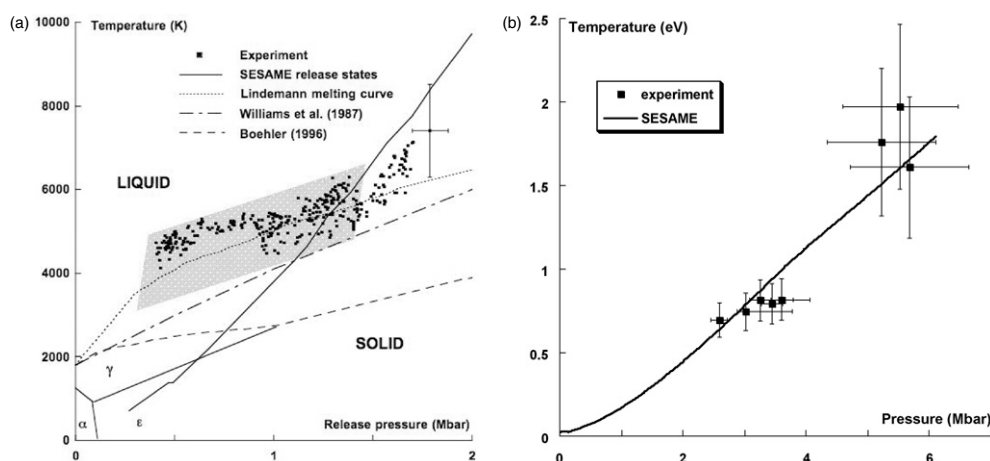
Figure 3. (*a*) Experimental time-resolved release temperature data. The grey zone corresponds to the crossing of the melting line. (*b*) Experimental Hugoniot temperature data.

Another possible mechanism that would explain the anomalous velocity behaviour rests on the LiF index of refraction as a function of compression. Indeed, Kormer's model has been experimentally tested up to 1.15 Mbar which is below the pressure range of interest in our experiments (1.5–3 Mbar). Earlier work by Russian groups have shown that the $\mathrm{d}n/\mathrm{d}\sigma$ term increases by a factor 1.5–1.7 for ionic crystals CsBr, KCl and KBr undergoing a shock-induced solid–liquid transition. A similar behaviour can be expected from LiF, provided it would become liquid around 1.5 Mbar, which would lead to a sensible decrease in the apparent interface velocity.

To determine the temperature around the melting curve, we used the same self-emission diagnostic, as used for water, described in the previous section. We used reflectivity along with self-emission data to provide grey body equivalent temperature measurements. Release and shock temperature data as a function of pressure are discussed now.

2.2.1. Release temperature. From simultaneous, time-resolved interface velocity and self-emission measurements we obtained temperature versus pressure data for iron upon partial release for two laser shots (figure 3(*a*)). In both cases, as pressure decreases, temperature drops sharply before going through a plateau-like phase. We attribute this plateau to the coexistence of solid and liquid phases, as iron crosses the melting line during its release. Indeed, our data are best fitted by a Lindemann melting law in which the Grüneisen parameter is set to 1.85.

Extrapolation of the melting data along the Lindemann curve yields 7800 ± 1200 K as a melting temperature at IOB (3.3 Mbar). This is in good agreement with previous dynamic works on iron [21, 22]. However, the discrepancy between static [23] and dynamic works still stands: our melting curve is located about 2000 K higher than static measurements. In a recent work [24], Luo and Ahrens suggest that this discrepancy might be due to superheating. This phenomenon can occur regardless of heating rate. However, it is seldom observed at low heating rates as free surface effects dominate. In [24], superheating is calculated at 10^{12} K s^{-1} heating rate, which is typical of shock loading. According to this theory, iron could be shock-heated up to 23% above its melting temperature and remain in a solid state.

2.2.2. Shock temperature. The Hugoniot for iron in the pressure–temperature plane (figure 3(*b*)) was calculated using the Mie–Grüneisen relationship:

$$T_{\text{shock}} = T_{\text{release}} \exp \left[\int_{V_{\text{shock}}}^{V_{\text{release}}} \frac{\gamma}{V} \mathrm{d}V \right],$$

where $\gamma = V \mathrm{d}p/\mathrm{d}E$ (p is pressure, E is internal energy) is the Gruneisen parameter and $\gamma/V = 19.6$ from [14].

Because self-emission signals are very weak in the case of iron, only the stronger shock data could be analysed. These data are found to be in the liquid phase, preventing comparison with previous measurements [21,22]. Nevertheless, we find good agreement with the SESAME EOS, which allows us to validate the measurement technique.

In future experiments, temperature measurements in the solid phase will require a lower threshold diagnostic such as infrared self-emission. In order to provide evidence of superheating, it would be interesting to combine self-emission diagnostics with x-ray based techniques, in order to verify the presence of a crystalline structure.

3. Recent developments

One of the most open questions in the laser driven shock wave community is to have comparable error bars with the high pressure community which uses static compression. This implies the development of new diagnostics capabilities mainly focused on parameters other than the hydrodynamic ones, i.e. the shock and fluid velocities; among the parameters to be measured, density is one of the most important. Indeed in all previous experiments, density has be deduced from the Rankine–Hugoniot relations given by equation (1), and errors bars can be therefore quite large (see [5]). One of the possibilities is to use backlighter source of either protons or hard x-rays. We present, in the next section, recent experiments designed to check these new techniques and their accuracy.

3.1. Proton radiography

In order to determine the material density compressed by a shock, we performed an 'exploratory' experiment using high-energy protons to characterize *in situ* the spatial and temporal evolution of a laser-driven shock propagating through a low-Z material. The shock strength was inferred from shock velocity measurements using VISAR. The transverse high-energy proton beam (with energy up to 10 MeV) was generated focusing a short intense laser beam (350 fs, $\sim 3 \times 10^{19}$ W cm^{-2}) on a 'backlighter foil'. Proton bursts produced from high-intensity laser foil interactions [25–27] have extremely good emittance and short ($\sim$picoseconds) duration, allowing excellent spatial and temporal resolution when used as a particle probe in a point-projection scheme [28, 29]. Up to now such beams have been used to probe highly transient electric fields in underdense plasmas or at the surface of laser-irradiated targets. Experiments similar to the one described here, but in a different context, have been conducted using high explosives to drive a shock in a metal and a high energy proton beam (800 MeV) from conventional accelerators to probe it [30].

In order to perform our experiment, we used the 100 TW LULI laser where the chirped pulse (80 J, 500 ps at $\lambda = 1064$ nm) generated a shock in a pusher ($P \approx 5$ Mbar). In order to minimize scattering effects, we designed the target as shown in figure 4. The ablator–pusher layer was formed by 4–6 μm of CH and 25 μm of aluminium. Then a thin sliver (150 μm in the proton beam direction) was glued on this foil. We present here some preliminary results and discuss the possibilities of this new technique.
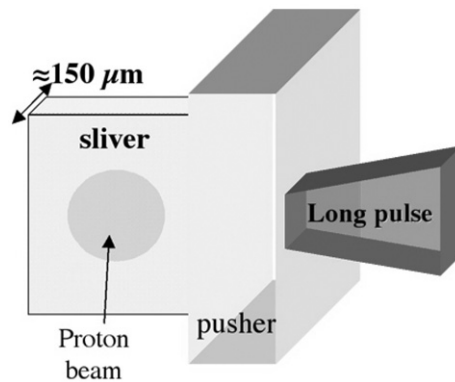
Figure 4. Proton radiography target scheme.

Among the different shots we performed on the low-Z transparent materials (Lexan, quartz, diamond, LiF), the quartz case represents a paradigm, the sliver quality being excellent and the results corresponding to a typical trend. Figure 5(a) shows a 6 Mev proton image of the shock propagating in the quartz sliver. In this image, only half of the proton beam is observed, the other half being cut by the ablator–pusher part and the target holder. In the rectangular part representing the sliver, the protons are slowed down while they are propagating through the quartz inducing a beam intensity decrease. However, the high compression induced by the shock wave was not observed even for the highest proton energy (≈ 10 MeV). Simulations of the proton radiograph have been carried out with a code (MPRM) [31] based on the Monte carlo TRIM package using a density profile given by a 1D simulation (see figure 5(b)) and assuming that the shock extends transversely across the whole sliver thickness. The MPRM code simulates the scattering and stopping undergone by the probe particles both in the radiographed target and in the detector and employs a multi-energy proton beam (in this case a Boltzmann energy distribution with $T = 1.5$ MeV).

The experimental projection arrangement and detector pack composition were used. The simulations reveal that, in the conditions of figure 5(a), the energy of the protons was insufficient to produce, in correspondence to the shocks, a visible modulation in the dose deposited over the RCF. Indeed, the difference in energy lost by protons passing through the uncompressed and compressed matter can significantly modulate the proton density profile in the beam cross-section: this is observed in simulations where the detector was placed in contact with the target, an experimentally impractical arrangement due to the lack of magnification and the detector proximity to the target. When the detector is located at a distance of a few centimetres from the target, resolution blurring due to scattering in the target takes over and smoothes out the density dip, making it irresolvable in the detector dose profile. Further calculations were carried out in order to evaluate whether the shock could be detected in this experimental arrangement, by employing higher energy protons, which would suffer less scattering. In order to achieve this, the code calculated the dose deposited on RCF films located later in the film pack, where the Bragg peak is reached by higher energy protons. MPRM simulations predict that, by employing protons of energy exceeding 10 MeV, one would be able to reveal the presence of the shock wave inside the sliver in the experimental conditions of figure 5(a). Further increasing the proton beam energy (and correspondingly the beam temperature) can significantly improve the modulation in the dose profile and hence the resolution of the radiography as shown in figure 5(b).
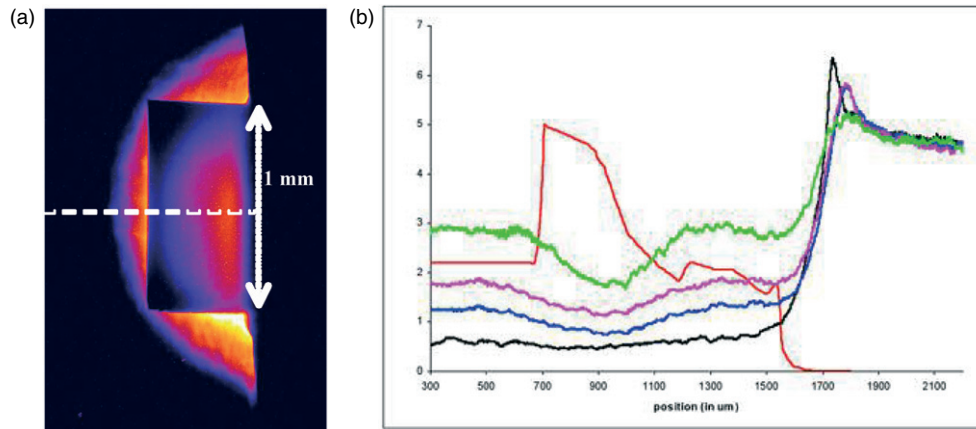
Figure 5. (*a*) Proton image of a shock propagating into a quartz sliver. The square shadow corresponds to the proton absorption in the sliver and the bright circle to the protons around it. (*b*) Simulated dose profile obtained for a density profile given by 1D simulation (red). The Bragg peak energy E_p for the selected RCF layer and the beam temperature T used are as follows: black— $E_p \sim 7\,\text{MeV}$ and $T = 1.5\,\text{MeV}$; blue—$E_p \sim 12\,\text{MeV}$ and $T = 1.5\,\text{MeV}$; pink—$E_p \sim 12\,\text{MeV}$ and $T = 3\,\text{MeV}$; green—$E_p \sim 22\,\text{MeV}$ and $T = 3\,\text{MeV}$. The x coordinates are rescaled to a fixed magnification. The background dose level in all lineouts have been renormalized.

3.2. X-ray radiography

As mentioned previously, many EOS studies rely on impedance matching to a known standard, but at high pressures ($P \geqslant 5\,\text{Mbar}$) uncertainties in the EOS of that standard material (such as aluminium) ultimately limit the accuracy of such a technique. Previous efforts to perform absolute EOS measurements using time-resolved x-ray radiography were limited by the extreme precision required to measure shock and particle velocities at such high compressions [5]. The other option is to infer the shocked density directly with x-ray radiography, which can be done in a 'classical way' using long pulse beams or with new techniques involving ultra-intense short pulse beam. For the former, one has to deal with thermal radiation which implies that the x-ray photon energy we are dealing with is always lower than 10 keV. Recent experiments on the OMEGA laser system have employed a new technique designed to achieve direct density measurements in a shock wave. Side-on radiography using point-projection imaging ($\approx 5\,\text{keV}$ x-rays) was used to produce a snapshot of the expanding shock wave; this 2D image was then tomographically inverted to determine the density profile behind the shock front. By simultaneously measuring the shock velocity using VISAR, absolute EOS points were determined. This technique conveniently scales to measurements on higher-Z materials using harder x-rays from an intense short-pulse laser. Indeed a very hard x-ray Kα source (20–100 keV) can be produced by relativistic electrons generated by the interaction of an ultra-intense laser beam with solid target [32]. Such an experiment is currently underway on the VULCAN laser at the Rutherford Appleton Laboratory.

References

[1] N R Council 2003 Frontier in High Energy Density Physics (Washington: The National Academy Press)
[2] Car R and Parrinello M 1985 *Phys. Rev. Lett.* **55** 2471
[3] Mermin N 1965 *Phys. Rev.* **137** A1441
[4] Kohn W and Sham L J 1965 *Phys. Rev.* A **140** 1133

 [5] Collins G *et al* 1998 *Science* **281** 1178
 [6] Huser G *et al* 2005 *Phys. Plasmas* **12** 060701-1
 [7] Koenig M *et al* 1998 *Appl. Phys. Lett.* **72** 1033
 [8] Celliers P M *et al* 1998 *Appl. Phys. Lett.* **73** 1320
 [9] Collins G W *et al* 2001 *Phys. Rev. Lett.* **87** 165504-1
[10] Boehler R 1993 *Nature* **363** 534
[11] Al'tshuler L V *et al* 1958 *Sov. Phys.* JETP **7** 606
[12] Krupnikov K K *et al* 1963 *Sov. Phys. Dokl.* **8** 205
[13] Trunin R F *et al* 1992 *Sov. Phys. JETP* **75** 777
[14] Brown J M and McQueen R G 1986 *J. Geophys. Res.* **91** 7485
[15] Laio A *et al* 2000 *Science* **287** 1027
[16] Zeldovich Y B and Raizer Y P 1967 *Physics of Shock Waves and High Temperature Hydrodynamic Phenomena*
        (New York: Academic)
[17] 1992 *SESAME: The LANL Equation of State Database* LA-UR-92-3407, Los Alamos National Laboratory
[18] Wise J L and Chhabildas L C 1985 *Shock Wave in Condensed Matter (Spokane)* p 441
[19] Poirier J P 1986 *Geophys. J. R. Astron. Soc.* **85** 315
[20] Anderson O L and Duba A 1997 *J. Geophys. Res.* **102** 22659
[21] Yoo C S *et al* 1993 *Phys. Rev. Lett.* **70** 3931
[22] Williams Q *et al* 1987 *Science* **236** 181
[23] Boehler R 1996 *Phil. Trans. R. Soc. Lond.* **354** 1265
[24] Luo S N and Ahrens T J 2003 *Appl. Phys. Lett.* **82** 1836
[25] Clark E L *et al* 2000 *Phys. Rev. Lett.* **84** 670
[26] Snavely R A *et al* 2000 *Phys. Rev. Lett.* **85** 2945
[27] Roth M *et al* 2002 *Plasma Phys. Control. Fusion* **44** B99
[28] Borghesi M *et al* 2003 *Appl. Phys. Lett.* **82** 1529
[29] Borghesi M *et al* 2002 *Phys. Plasmas* **9** 2214
[30] Holtkamp D *et al* 2003 *Shock Compression of Condensed Matter (Portland,Or, USA)* p 477
[31] Kar S *et al* 2004 Modelling of proton radiography of cold matter *Central Laser Facility Annual Report* 2003/2004,
        RAL-TR-2004-025, 26 CCLRC
[32] Park H-S *et al* 2004 *Rev. Sci. Instrum.* **75** 4048